

Sylva

CNRS - Université Pierre et Marie Curie - Université Versailles-Saint-Quentin
CEA - ORSTOM - Ecole Normale Supérieure - Ecole Polytechnique

Institut Pierre Simon Laplace

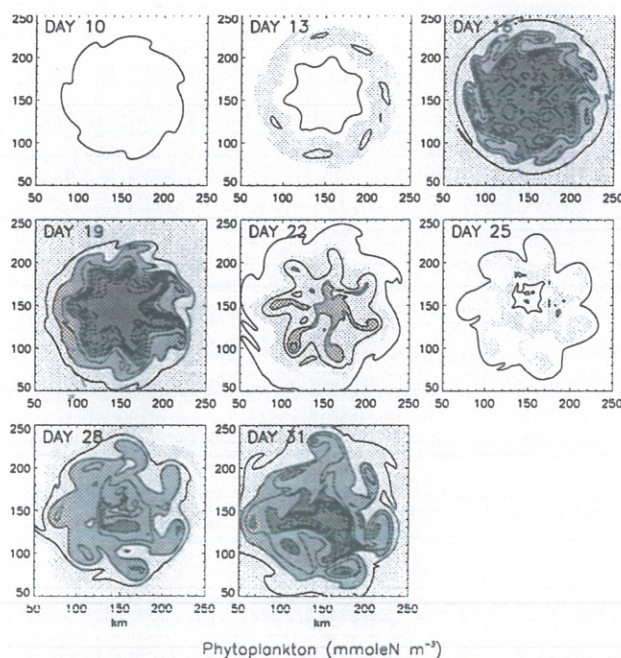
des Sciences de l'Environnement Global

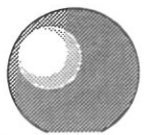
Notes du Pôle de Modélisation

Combined Effects of Mesoscale Processes and Atmospheric High-Frequency Variability on the Spring Bloom in the MEDOC Area.

Marina Lévy, Laurent Mémerly and Gurvan Madec

Laboratoire d'Océanographie DYnamique et de Climatologie
CNRS / PARIS 6 / ORSTOM



 I P S L	CNRS - Université Pierre et Marie Curie - Université Versailles-Saint-Quentin CEA - CNES - ORSTOM - Ecole Normale Supérieure - Ecole Polytechnique
	Institut Pierre Simon Laplace des Sciences de l'Environnement Global
	CETP - LMD - LODYC - LPCM - LSCE - SA
	<div> <div> Université Pierre-et-Marie-Curie B 102 - T15-E5 - 4, Place Jussieu 75252 Paris Cedex 05 (France) Tél : (33) 01 44 27 39 83 Fax : (33) 01 44 27 37 76 </div> <div> Université Versailles-Saint-Quentin College Vauban, 47 Boulevard Vauban 78047 Guyancourt Cedex (France) Tél : (33) 01 39 25 58 17 Fax : (33) 01 39 25 58 22 </div> </div>

Combined Effects of Mesoscale Processes and Atmospheric High-Frequency Variability on the Spring Bloom in the MEDOC Area.

Marina Lévy, Laurent Mémery and Gurvan Madec

Laboratoire d'Océanographie DYnamique et de Climatologie
CNRS / PARIS 6 / ORSTOM

Une étude de modélisation est menée dans le but de comprendre les processus responsables de la variabilité spatio-temporelle du déclenchement et du déclin de la floraison printanière en Méditerranée nord-occidentale (zone MÉDOC). La démarche suivie est d'isoler artificiellement les sources de variabilités dans l'océan et dans l'atmosphère qui sont susceptibles d'avoir un impact sur la floraison (dynamique océanique à mesoechelle, réchauffement printanier, coups de vents), et ce au niveau du forçage du modèle biogéochimique. On dispose alors d'une série d'expériences (no flux, warming et wind), sur la base desquels les processus sont étudiés individuellement, ce qui permet l'analyse d'une expérience plus réaliste, forcée par des données atmosphériques journalière (expérience high-frequency). Cette étude nous permet de proposer une catégorisation des processus impliqués dans la floraison printanière, en termes de leurs impacts sur son déclenchement et son déclin, et des échelles spatiale et temporelle sur lesquelles ils jouent.

Juin 1998
Note n° 7

Combined Effects of Mesoscale Processes and Atmospheric High-Frequency Variability on the Spring Bloom in the MEDOC Area.

Marina Lévy, Laurent Mémery and Gurvan Madec

LODYC, CNRS / PARIS 6 / ORSTOM

marina@lodyc.jussieu.fr
memery@lodyc.jussieu.fr
madec@lodyc.jussieu.fr

Laboratoire d'Océanographie Dynamique et de Climatologie
Université Pierre et Marie Curie
5, place Jussieu
75252 Paris Cedex 05
France
fax: (33) 1 44 27 71 59

Submitted to Deep Sea Research, June 1998

ABSTRACT

A number of processes are proposed to explain the time and space variability of the onset and decay of the spring phytoplankton bloom. This is done in the modeling framework of a case study most representative of the northwestern Mediterranean Sea (MEDOC area). The strategy followed is to isolate the different possible sources of variability (oceanic mesoscale dynamics, spring warming, wind bursts) in a series of process experiments (*no flux*, *warming* and *wind* experiments). The analysis of these experiments provides information for the analysis of a more realistic experiment, forced with daily atmospheric data (*high-frequency* experiment). On the basis of this study, we propose a categorization of the processes that control the spring bloom, in terms of their impact on the onset and decay of the bloom, and of the time and space scales on which they apply.

INTRODUCTION

It has been recognized for decades that the restratification of the water column is a prerequisite for the onset of spring phytoplankton blooms in offshore waters of temperate regions (Gran and Braarud, 1935 ; Sverdrup, 1953). The most classical scenario is that nutrients are brought to the surface during winter mixing, and are then continuously utilized during spring, when the water column becomes more stable. However, studies in the Mediterranean Sea and in the North Atlantic provide evidence for commencement of blooms prior to seasonal restratification (Garside and Garside, 1993 ; Marty, 1993 ; Townsend *et al.*, 1992), as well as for variable bloom timing (André, 1990 ; Townsend *et al.*, 1994 ; Williams, 1988). The modeling study of Townsend *et al.* (1994) showed that the spring bloom can begin following the winter period of convective mixing, and prior to the vernal development of vertical water column stability, provided that the wind speed and the cloud cover are both weak enough. Restrartification induced by mesoscale eddies is another way to sustain the onset of a bloom prior to the spring restratification, as emphasized by the modeling study of Lévy *et al.* (1998a, hereafter referred as LMM).

In the Mediterranean Sea and the North Atlantic, the depletion of nutrients is the process commonly evoked to explain the bloom decay (Garside and Garside, 1993 ; Jacques *et al.*, 1976). However, continuous records (Marra, 1995) and time series (Williams, 1988) of phytoplankton clearly show that the spring bloom does not always consist of a single steady increase of phytoplankton until surface nutrients are depleted, but must often consists of several spring bloom pulses. Townsend *et al.* (1994) argue that a vertical mixing event following the uptake of some portion of the available nutrient could cause the bloom to crash, and at the same time serve to replenish the surface nutrient field, thus allowing a subsequent bloom to occur. Essentially at the beginning of spring, when the water column is weakly stabilized, a wind burst is sufficient to initiate such an event. On the other hand, the study of McGillicuddy and Robinson (1997) in the oligotrophic Sargasso Sea has shown that eddies can advect a significant amount of nutrients to the depleted surface. In consideration of the strong eddy variability shown by the spring sea-color images in the Mediterranean Sea (André and Morel, 1991) or in the North Atlantic (Robinson *et al.*, 1993), it is conceivable that eddies continue to enrich the surface when it is not yet depleted, leave their signature on the surface phytoplankton field, and locally delay the decay of the bloom.

The present consensus on the spring bloom is therefore no longer to consider it as a steady phenomenon, but as a phenomenon that shows strong space and time variabilities, from its first onset to its final decay. Previous modelling studies strongly suggest that attempts to predict primary productivity during the bloom will be inaccurate if small scale processes such as wind bursts or eddies are not taken into account. For instance, Lévy *et al.* (1998b) estimated that the eddy effect on the shoaling of the mixed layer could increase productivity by up to a factor of four during the onset of the bloom in the Mediterranean Sea (before the heat budget at the ocean surface has become positive). McGillicuddy *et al.* (1995) showed that vertical velocities associated with mesoscale eddies could enhance nutrients by one order of magnitude during the spring bloom in the North Atlantic, and therefore substantially increase productivity in localized regions for periods of weeks. Using a one-dimensional ecosystem model forced with a prescribed mixed layer near Bermuda,

Bisset *et al.* (1994) highlighted that using monthly instead of daily mixed-layer estimates could lead to a 25% under-estimation of new production.

Within this context, the aim of this paper is to study the joint impact of mesoscale activity, spring warming and wind bursts on the onset and decay of the spring phytoplankton bloom. This is done in the modeling framework of a case study most representative of the northwestern Mediterranean Sea (MEDOC area). This region is one of the few in the world's oceans where deep water formation occurs (Medoc group, 1970) ; during winter, a deep-mixed patch of dense water is formed, whose breakup involves mesoscale eddies (Gascard, 1978). The situation explored in this work is the period of sinking and spreading of this dense water patch, characterized by important eddy activity. During that period, the air-sea heat budget shows a mean seasonal trend from strong winter buoyancy losses (which drive deep convection) to spring warming (which builds up the seasonal thermocline). This mean trend is perturbed by strong wind bursts (Mistral, Tramontane) associated with large heat losses (For instance Fig. 1, end of February and end of March). In a previous study dedicated to the understanding of the spring bloom variability in the MEDOC region (LMM), these highly variable fluxes were not considered in order to isolate and understand the sole impact of the mesoscale eddy dynamics on primary production during the onset of the bloom, before nutrients are depleted. In this second paper, the role of the atmospheric forcing over this period of very energetic eddy dynamics is investigated. A set of experiments of increasing complexity is presented and analyzed. The main results obtained in LMM are first briefly summarized. Next, the impact of the spring increase of solar radiation is assessed, which permits to investigate the decay of the bloom and the role of mesoscale eddies during this decay. We then discuss the effects of the Ekman transport induced by a constant wind. Finally, in order to analyze the impact of the high-frequency variability of the atmospheric forcing on the spring bloom, real forcing are used ; the analyze relies on the results of the previous experiments and on in situ data.

DESCRIPTION OF THE EXPERIMENTS

The model, the basin configuration, the initial conditions and the spin-up are identical in all experiments. The model consists of a NPZD (Nutrient, Phytoplankton, Zooplankton, Detritus) biogeochemical model (described in the Appendix), embedded in an eddy-resolving primitive equation ocean model (Madec *et al.*, 1991a ; Delecluse *et al.*, 1993). Vertical eddy coefficients are computed from an embedded 1.5 turbulent closure model (Blanke and Delecluse, 1993). The Eulerian time evolution of any of the four biogeochemical variable C is controlled by biogeochemical processes $S(C)$, advection and vertical diffusion :

$$\frac{\partial C}{\partial t} = S(C) + \nabla \cdot (UC) + \frac{\partial}{\partial z} \left(k_z \frac{\partial C}{\partial z} \right) \quad (1)$$

where U , the velocity vector, and k_z , the diffusion coefficient, are computed by the physical model. A positive definite transport scheme is used for the advection of biological tracers (Smolarkiewicz and Clark, 1986). This scheme is slightly diffusive, so that no explicit horizontal diffusion operator is used.

The domain is a closed basin of 300 km x 300 km x 2500 m. The initial state is composed of a patch of dense water ($\sigma_\theta=29.1$), extending from the surface down to the bottom and surrounded by a stratified ocean, which is characteristic of the winter situation (Medoc group, 1970 ; Leaman and Schott, 1987). The density of the stratified area is homogeneously set to $\sigma_\theta=28.4$ over the first 80 m, and gradually increases to the value of 29.1 at the bottom. The first three Rossby radius of deformation corresponding to this density profile are 8.4, 3.8 and 2.5 km. Therefore, in order to resolve the baroclinic mesoscale eddies, the horizontal grid spacing is set to 2.5 km. The vertical grid spacing varies from 10 to 25 m in the upper 130 m, and reaches 500 m near the ocean bottom. The time step is 8 minutes.

All experiments start at day nine, after a dynamical spin-up phase of eight days, and are performed for twenty-five days after the spin-up phase. The initialization of the biogeochemical variables is done after the spin-up phase. High density (in the center of the convective region) is correlated with high nitrate and

low phytoplankton concentrations according to Coste *et al.* (1972) and Jacques *et al.* (1973), such that nitrate and phytoplankton concentrations in the denser waters are 6 and 0.01 mmole m⁻³ respectively, while they worth 1 and 0.1 mmole m⁻³ in the lighter waters. Zooplankton and detritus are uniformly set to low values, 0.015 and 0.1 mmole m⁻³, respectively.

Experiments differ by the atmospheric forcings applied (Table 1). Atmospheric forcings consist of a net heat flux, split up into a penetrative solar heat flux and a non-penetrative flux, and wind stress. They are applied after the spin-up phase, with no space variation, which is a reasonable approximation considering the small horizontal extent of the domain. In the experiment presented in LMM, both the penetrative and the non-penetrative parts of the heat flux are kept constant in space and time, and compensate each other (+150 and -150 W m⁻², respectively). The net heat flux is thus zero, and there is no wind ; the main sources of vertical mixing are therefore the static instabilities generated by the penetration of the solar radiation. Below, this experiment will be abusively referred as the *no flux* experiment, whereas in fact it is a no net flux experiment.

Meteorological models indicate that the increase of the solar heat flux during February and March in the Medoc area has a mean trend of 2W m⁻²d⁻¹. During the same period, the non-solar flux presents a high-frequency variability related to the occurrence of wind bursts (Fig. 1). In order to account for the impact of the mean spring warming, a *warming* experiment is performed where the model is forced with an increasing solar heat flux, which has an initial value of 150 W m⁻² and a constant trend of 2W m⁻² d⁻¹, and a constant non-solar heat flux of -150 W m⁻² (i.e. the same value as in the *no flux* experiment). The net surface flux thus increases linearly with time from 0 to 70 W m⁻², while the wind stress remains zero.

In order to assess the impact of the wind stress, a *wind* experiment is performed, forced by the same heat forcing as in the *no flux* experiment and by an additional non-zero wind stress. This wind is oriented in the SE direction (i.e. the direction of the Mistral wind), thus minimizing the amplitude of the coastal Kelvin waves. Its magnitude is 0.15 Pa, corresponding to an average value for a wind burst

in winter (i.e. Fig. 1). This forcing is somehow unrealistic, as the strong heat losses often associated with Mistral burst are not taken into account and as the wind stress is applied during a whole month while a wind burst rarely exceeds a week. This is deliberately done in order to solely study the impact of the wind induced Ekman transport. The possible effects of Ekman pumping on productivity (Williams and Follows, 1998 ; Andersen and Prieur, 1998) are not addressed in this study.

Finally, in order to take into account all the variability of the atmospheric forcing, a *high-frequency* experiment is performed, where the model is forced with the daily ECMWF heat fluxes and wind stress over the MEDOC area from February 20 to March 15, 1990 (Fig. 1). This period is characterized by three wind bursts, the first one between days 17 and 18 of the experiment, the second one between days 19 and 23, and the third one between days 27 and 29. These typical Mistral wind bursts are oriented in the SE direction. The first and third ones have the same magnitude as the wind of the wind experiment. The second one is the most intense, and is associated with important heat losses (-400 Wm^{-2}). The time integrated heat flux exchanged with the atmosphere over the 25-day model run is the same as in the *warming* experiment. However, unlike in the *warming* experiment, the warming is not gradual ; it is much more intense between days 9 to 18 and 23 to 33, and is interrupted by a period of heat loss.

MESOSCALE DYNAMICS IMPACT

The impact of the mesoscale dynamics on the onset of the spring bloom is fully described in LMM. The main results of this study are summarized below. These results are based on the analysis of the *no flux* experiment. From a dynamical point of view, the main features of the collapse and spreading of a dense water patch are reproduced by the experiment : due to the steep slope of the isopycnals at the edge of the dense water patch, and to the relevant shears in the velocity field, the initial situation is unstable (Pedlosky, 1987) ; the release of the available potential energy contained within the dense-water patch occurs through the development of mixed barotropic-baroclinic instabilities. The signature of these instabilities on the

surface density field appears in the form of meanders along the front that defines the neutrally stable column. A time series of the surface density field (Fig. 2) shows the development of seven meanders at the outer edge of the convective region (day 12) having wavelengths of $\sim 50 \text{ km}$ (corresponding to the first baroclinic mode of oscillation), which eventually break into seven cyclonic eddies. Such meanders have been observed by *in situ* measurements (Gascard, 1978 ; Gaillard *et al.*, 1997) and their role in the sinking and spreading of the initial chimney was emphasized by the modeling study of Madec *et al.* (1991a). Basically, they serve as vehicles for the transfer of water masses, by sinking the denser waters out of the convective zone and at the same time upwelling lighter peripheral waters towards the center. Consequently, these mesoscale instabilities are responsible for the collapse of the dense water patch in approximately one month, in agreement with the restratification time scale estimated from Jones and Marshall (1997). Furthermore, they are associated with strong mesoscale upward motions (tens of meter per day) that are responsible for the shoaling of the mixing layer in the trough of the meanders (Fig. 3). As sunlight is the main factor regulating primary production during the onset of the bloom, this shoaling increases the mean exposure time of the phytoplankton cells and thus enhances productivity. Consequently, the majority of primary production is obtained in the areas of shallow mixed-layer, i.e. essentially at the edge of the patch. However, mesoscale instabilities are also responsible for a rearrangement of phytoplankton distributions ; following the water mass circulation, phytoplankton is transported from the trough towards the crest of the meanders, which explains the observed crest-like phytoplankton distribution (Fig. 4). This rapid transport (a couple of days) decorrelates phytoplankton biomass and primary production.

SPRING WARMING IMPACT

The impact of the spring warming is assessed by comparing the *warming* experiment with the *no flux* experiment. In the *warming* experiment, the response to the uniform warming is non-symmetrical. Indeed, the peripheral stratified waters are warmed more easily than the homogeneous central patch ; as a consequence, the horizontal density gradient between these two areas is increased, which increases the

unstable nature of the flow, in agreement with the hypothesis of Strass *et al.* (1992). This effect is weak, as the heating only affects the first layers, and only slightly modifies the overall slope of the isopycnals and the associated Rossby radius of deformation. However, it explains that the instabilities are not affected when a uniform warming is applied (Fig. 2). Madec *et al.* (1991b) report an opposite response to a homogeneous thermohaline forcing applied over a dense water patch ; in their case, a uniform cooling was responsible for a significant delay in the development of the instabilities, as the forcing was affecting deeper layers.

By contrast, the increase of the solar heat flux progressively and globally warms the surface waters of the basin, resulting in the formation of a seasonal thermocline over the convective area. In the *warming* experiment, the restratification of the water column is thus the result of two different processes : the *dynamical* restratification induced by the action of the mesoscale instabilities, and the *thermal* restratification achieved by the solar warming of the surface waters. As the warming has little effect on the instabilities, the *thermal* and *dynamical* restratifications are complementary rather than competitive, and restratification occurs more rapidly (about one week compared to one month over the convective site). The mixing-layer depth time series illustrates this result (Fig. 3) ; the mixing layer maintains the spatial structure imposed by the mesoscale motions, and in addition is globally shallower and shallower, which weakens the amplitude of its mesoscale variability. For instance, in the *no flux* experiment (day 32), the mixing layer is still deep in the central convective region (>100 m), and between 20 and 70 m at its periphery, while in the *warming* experiment it is always shallower than 50 m, and ranges between 20 and 40 m in the periphery region.

As productivity during the onset of the bloom is controlled by the depth of the mixing layer, this faster and stronger restratification has the effect of increasing productivity. This is illustrated by the comparison of the averaged productivity time evolution for the *warming* and the *no flux* experiments (Fig. 5). A second reason for the higher productivity levels observed in the *warming* experiment is the increase of the solar radiation, and therefore of the amount of light available for photosynthesis.

The comparison of the two phytoplankton time series (Fig. 4) shows that this higher productivity gives rise to significantly higher phytoplankton concentrations. On the other hand, the warming has little effect on the mesoscale distribution of phytoplankton. Indeed, as emphasized by the *no flux* experiment, the phytoplankton distribution is highly constrained by the transport through the instabilities, from the trough towards the crest of the meanders. The similar structures in the phytoplankton distributions between the two experiments thus results from the similarity in the dynamics of the instabilities.

In both experiments, the increase of the averaged productivity (i.e. the onset of the bloom) is followed by a decrease, marking the beginning of the bloom decay (Fig 5). However, this decrease has different origins in the two experiments. In the *no flux* experiment, the decay results from the diminution of the mixing-layer depth variance with time, in relation to the progressive dissipation of the instabilities. In other words, the productivity diminishes because the spatial extend of the productive areas (areas of minimal mixing-layer depth) diminishes with time (Fig. 3). In the *warming* experiment, the thermodynamic restratification causes the average mixing-layer depth to strongly decrease during the course of the experiment (Fig. 3) ; as a result, vertical mixing becomes less limiting. On the other hand, nutrients are exhausted faster during the bloom onset because productivity is more intense (Fig. 5). This creates a nutrient stress on productivity, which is not the case in the *no flux* experiment. Surface nutrient concentration time series for the two experiments (Fig. 6) show that nutrient concentrations remain higher than the half-saturation constant (0.5 mmole m^{-3}) during the whole duration of the *no flux* experiment, while they fall below this value by day 24 in the *warming* experiment. In the *warming* experiment, the bloom decay is thus clearly the result of a nutrient stress at the surface.

However, the depletion of nutrients in the *warming* experiment is not homogeneous (Fig. 6), and partly counter-balanced by the action of the instabilities. The nutrient surface field shows strong mesoscale variability, with maxima located within the eddies. These nutrient maxima are correlated to the density maxima (Fig. 2). They result from the vertical transport of dense, rich waters from below. In order to evaluate the importance of this vertical transport, the relative strengths of physical

and biological processes with regards to the nutrient concentrations are assessed. The biological (production minus remineralization) and dynamical (advection plus diffusion) terms of the surface nutrient time evolution equation (Eq. 1) are integrated over time and averaged over the circular band extending between 35 and 100 km from the center (delimited by the dashed lines on Fig. 6), which covers the instability area (Fig. 7). The results of this procedure are given in units of a nutrient concentration per cubic meter. The time integrated biological terms represent the amount of nutrient that would be obtained if the physical transport was cut off while keeping the same level of productivity (“biological” nutrients), while time integrated dynamical terms represent the amount of nutrient that would be observed if the biological activity was turned off, while keeping the same tracer gradients (“dynamical” nutrients). By construction, the sum of the “biological” and “dynamical” nutrients equals the actual surface nutrient concentration, which is also depicted on Figure 7 for comparison. The average surface concentration of nutrients in the instability area decreases from about 3 down to 0.1 mmoleN m⁻³ within a month. During that period, biological processes clearly tend to decrease the stock of nutrients (Fig. 7, dashed line), while dynamical processes tend to increase it (Fig. 7, dotted line). The overall decrease results from the faster consumption by productivity compared to the dynamical enrichment. The integrated input of nutrients at the surface by dynamical processes during the *warming* experiment is 1.8 mmoleN m⁻³, representing about 40% of the total biological utilization during the same period. Productivity during the bloom is thus strongly sustained by the dynamical input of nutrients that occurs in the instability region. Furthermore, our diagnostic shows that the dynamical input of nutrients has the effect of delaying the end of the bloom. Indeed, “biological” nutrients are totally depleted one week before the actual nutrients, meaning that the duration of the bloom is extended by one week by the fertilizing action of the instabilities.

WIND STRESS IMPACT

The impact of the wind stress is assessed by comparing the *wind* experiment with the *no flux* experiment. In the *wind* experiment, the wind generates an Ekman

transport in the top 50 meters from the NE (upper right) to the SW (lower left) of the domain, i.e. in the direction perpendicular to the wind direction. In the NE area, the wind-driven transport supplies the convective area with light surface fluid from the periphery. Vertical density gradients are enhanced, which weakens vertical mixing and contributes to restratify the convective site. This *Ekman* restratification is much more efficient than the *dynamical* restratification, and has a wider extend. In contrast, dense water originating from the convective site are spread over in the SW area. This generates static instabilities in the SW area and therefore vertical mixing. In this area, the Ekman flux thus works against the *dynamical* restratification. These results agree with those of Francks and Walstad (1997), who examined the effect of the Ekman transport at a non-meandering ocean front. They are illustrated by the mixing-layer depth field (Fig. 3). In the *wind* experiment, the mixing-layer depth minima are located at the intersection between the instability area and the NE half of the domain. They rotate to the north during the course of the experiment, because of the advection by the mean cyclonic current around the convective site. By contrast, in the SW half of the domain, the mixing-layer is deeper than in the *no flux* experiment (days 16 and 24). The mode seven signature of the instabilities is still clearly apparent on the surface density field (Fig. 2), although in the NE region, surface density gradients are weakened by the lateral mixing with lighter waters. This illustrates that contrary to the *warming* experiment, the dynamics associated with the instabilities is modified by the forcing, even though the modification is weak. The wind induced transport thus decorrelates the mixing layer from the action of the instabilities, slightly modifies the transport by the instabilities, but does not alter the mode of the instabilities.

Surface phytoplankton time series (Fig. 5) show that phytoplankton develops mostly in the NE area, where the mixing-layer is the shallowest. The primary effect of the Ekman transport on phytoplankton distribution is therefore to break its axial symmetry (as for the density field). In the convective area, the minima of phytoplankton rapidly vanish due to the fast *Ekman* restratification. The mean phytoplankton concentration is increased, as in the *warming* experiment, in response to this additional restratification. The typical feature of the phytoplankton

distribution in the *no flux* experiment, with a minimum at the center and a maximum around the convective area, is strongly altered ; at day 16, a biomass-rich area and a biomass-poor area are next to one another ; at days 24 and 32, maxima of biomass have shifted toward the center. Moreover, the mode seven signature of the instabilities is still clearly visible in the surface phytoplankton field, even though it is strongly damped in the mixing-layer depth field. This is particularly obvious at day 24, when the eddies are fully formed. Indeed, similarly to the *no flux* experiment, these mesoscale patterns in the phytoplankton field are due to the transport of phytoplankton by the instabilities.

Surface nutrients time series (Fig. 6) show no drastic nutrient depletion by the end of the *wind* experiment, as in the *no flux* experiment. However, concentrations in the NE area (between 0.5 and 1 mmole N m⁻³) are clearly smaller than concentrations in the SW area (> 1 mmole N m⁻³). Two processes explain the asymmetry. First, productivity is higher in the NE (because of the shallower mixing layer) and thus nutrients are more rapidly used. Second, in the SW area, the Ekman flux is directed from the cold side (rich in nutrients) to the warm side (poorer in nutrients). This flux is responsible for a lateral transport of nutrients, from the dense water patch to the SW. Such an enrichment of the surface layer by horizontal cross-frontal transport of nutrients by an Ekman flux has also been emphasized in the case of a non-meandering front (Francks and Walstad, 1997). It is much stronger than the enrichment by vertical diffusion of nutrients that wind-surface current interactions can induce (Klein and Coste, 1984) , and which is hardly perceptible here. The main effects of the wind induced Ekman transport are to break the symmetry of the problem, and in particular to modify the large scale distribution of phytoplankton, without altering the wavelength of its mesoscale patterns. The Ekman flux is also responsible for a horizontal spreading of nutrients at the surface, which can have a significant implication in the productivity budget, as shown in the next section.

CASE WITH A REALISTIC FORCING

The case with a realistic forcing is explored in the *high-frequency* experiment. Until the first wind burst (day 17), the dynamical characteristics are similar to those of the *warming* experiment, except with a stronger warming and a faster restratification : the surface density time series (Fig. 8a) clearly show the presence of instabilities, and the lightening of the surface waters. The time series of the density section across the basin (Fig. 8b) illustrate the fast restratification over the convective area (days 10 to 16). Soon after the beginning of the first warming period (days 13 to 16), the mixing layer is homogeneously shallower than 15 m (Fig. 9). The first wind burst distorts the surface density meanders, and deepens the mixing layer in the SW area (day 19). This asymmetrical deepening is the result of the Ekman transport, as emphasized by the *wind* experiment. Between days 19 and 25, the strong heat loss erodes the central area, which is less stratified than the peripheral area, and reinitiates deep convection. The surface waters are cooled, the central zone is homogenized, and the mixing-layer deepens. Minima of mixing-layer depth appear in the meander trough, as in the *no flux* experiment. Note that the surface density meanders have recover their initial axial symmetry, illustrating that the distortion induced by the wind did not occur below a certain depth (~ 50 m), in agreement with Ekman's theory. Starting from day 25, the system warms up again. The impact of the third wind burst is perceptible in the NE-SW asymmetry of the mixing-layer depth at day 28 (Fig. 9).

Figure 10 shows the time series of the surface phytoplankton concentration and of the phytoplankton vertical distribution across the basin. Because of the rapid restratification (days 10 to 16), phytoplankton grows very intensely. Maximum concentrations are first found at the edge of the convective site (day 13), where restratification starts, and then shift toward the center (richer in nutrients, day 16), as in the *no flux* experiment, only much faster. Between days 19 and 25, during the second wind burst, surface concentrations strongly decrease, particularly at the center of the domain ; phytoplankton, which was confined to a thin surface layer, is detrained at depth by the deepening of the mixing layer. The detrainment does not damp the phytoplankton mesoscale variability ; indeed, as in all experiments,

mesoscale variability in the phytoplankton field is created by the mesoscale transport of the cells. From day 25, restratification enables the start of a second bloom. Again, phytoplankton starts developing at the border of the convective site ; then maxima are both found at the center of the zone and within the eddies.

The *high-frequency* experiment therefore explores the consequences of the variability of the atmospheric forcing on the spring bloom within a peculiar scenario, where a strong wind burst associated with intense cooling perturbs the spring warming. Consequently, two bloom pulses are separated by a period of export. Figure 11 shows the time evolution of the averaged productivity and averaged phytoplankton and nutrient surface concentrations. The two blooms obviously appear on the phytoplankton and nutrient curves, which show the succession of two phytoplankton maxima correlated with nutrient minima. The averaged productivity evolution is more complex, and modulated by the three wind bursts in different ways. From day 9 to day 15, productivity increases. Compared to the *warming* experiment (Fig. 4), this increase is more abrupt because of the faster restratification. The depletion of nutrients on day 16 causes the first decrease of productivity. As in the *warming* experiment, this decrease is attenuated by the dynamical transport of nutrients to the surface through the instabilities. The lateral Ekman transport associated with the first wind burst on day 17 spreads nutrients initially confined within the central area, as emphasized by the *wind* experiment. This globally enriches the mixing layer in the SW in nutrients, and consequently increases production. The second wind burst starting on day 19 is responsible for intense vertical mixing that crashes the bloom, while fully replenishing the surface layer in nutrients. Production starts again on day 22, right after the wind has stopped to blow. The third wind burst on day 27 again provides new nutrients through Ekman transport, this time before the surface is completely depleted, which enhances productivity. Then productivity falls again by lack of nutrients, and is only sustained by the fertilizing action of the eddies.

The *high-frequency* experiment reproduces important general characteristics of the northwestern Mediterranean bloom : the total depletion of nutrients at the end of the bloom (Coste *et al.*, 1972 ; Marty, 1993), and the negligible role of zooplankton

grazing for one month after the bloom onset (Nival *et al.*, 1975) (not shown). Regarding phytoplankton surface concentrations (Fig. 10a), two opposite situations are alternatively simulated : a situation with a central poor area with local and eddy-like patches richer in pigments (days 10, 13 and again on day 25), and a situation characterized by a rich meandering central area, with concentrations reaching 5 mmoleN m⁻³ (days 16, 19 and again on days 22 and 25). Coastal Zone Color Scanner (CZCS) data analysis over the MEDOC area (André, 1990) show that these two opposite configurations are indeed observed during winter and spring. However, the *high-frequency* experiment evidences that they are associated with alternating periods of production and export, and are clearly related to the occurrence of the strong wind bursts. A wind event similar to the strong wind burst in the *high-frequency* experiment has been observed by Andersen and Prieur (1998) in May 1995 in the same area. They report a decrease of phytoplankton concentration during a wind burst, associated with significant particulate export, and followed by an increase of productivity that they attribute to an enrichment of nutrients by vertical mixing. Marra *et al.* (1990), Eppley and Renger (1988) and Hitchcock *et al.* (1987) also report comparable effects of the wind.

A comparison of the results of the *no flux* experiment with in situ and CZCS data is presented in LMM. However, because only space variability is accounted for in the *no flux* experiment, the validation is focused on the space phytoplankton distribution (typical patterns and wavelengths). Regarding space scales of variability, the present work showed that taking atmospheric forcings into account does not call these results into question ; indeed, the crest-like structures of the phytoplankton field result from the transport of phytoplankton by the instabilities, which are not very sensitive to the forcing. Furthermore, the surface phytoplankton field in the *no flux* experiment is characterized by the presence of a permanent thin band of maximum concentrations around the convective site (Fig. 5). This feature is validated in LMM by comparison with the in situ data of Nival *et al.* (1972) ; however, the fact that it has never been observed from space (André, pers. comm.) was puzzling. Now, with the results of the *high-frequency* experiment, we know that a variable atmospheric forcing makes this maximum phytoplankton band very

transient (it appears only on days 13 and 25), which can explain why it has been missed in the CZCS images.

DISCUSSION AND CONCLUSION

Several processes responsible for the variability of the spring phytoplankton bloom in the MEDOC area have been identified using the step-wise progression of model experiments. The strategy used was to isolate the different possible sources of variability (oceanic mesoscale dynamics, spring warming, wind bursts) in a series of numerical process experiments (*no flux*, *warming* and *wind*). The analysis of these experiments provided information for the analysis of a more realistic experiment (*high-frequency*), in which all the variability was accounted for. On the basis of these results, we propose a categorization of the processes that control the spring bloom in the MEDOC area, in terms of their impact on the onset and decay of the bloom, and of the time and space scales on which they apply.

The restratification of the water column is the necessary condition for the onset of spring blooms. This study has emphasized the role of three restratifying agents that work on different time and space scales. The *thermal* restratification is induced by the progressive increase of the solar radiation between winter and spring. It applies to large space and time scales (basin and season), but is also subject to high-frequency time variability (days), associated with the occurrence of wind bursts. The *Ekman* restratification results from the wind induced Ekman flux of light waters across a strong density gradient. It applies to medium space scales, typically the scale of a front (50 km), and on small time scales, given by the duration of a wind burst (2-3 days). The *dynamical* restratification is achieved by the mesoscale eddies that advect light waters over denser ones. It applies to small space scales, given by the scale of the eddies (20 km), and longer time scales, given by the decay time of the instabilities (1 month). Furthermore, *Ekman* and *dynamical* restratification can occur before vernal warming, and thus cause the bloom to start earlier in the season.

The decay of the bloom is subject to even more variability, as it can originate from the destratification of the water column or from the depletion of nutrients, but

can also be counter-balanced by further restratification and nutrient inputs. Again, a variety of time and space scales are in play. Destratification is progressive and applies to small space scales when it is associated with the decay of mesoscale instabilities (case of the *no flux* experiment). It is very sudden and applies to larger space scales when it is due to a strong wind bursts (case of the *high-frequency* experiment). However, in this case, the entrainment originating from the wind event is also responsible for an export of phytoplankton, and for the surface nutrient replenishment, which allows a second bloom to occur just after the wind burst. In the example of the *high-frequency* experiment, two bloom pulses are separated by a wind burst in that manner. Productivity before the strong wind burst is approximately 80 mmoleN m^{-2} (days 9 to 21, Fig. 11). Thirty percent of this production is exported during the wind burst, within 3 days. At the same time, the surface nutrient replenishment is 15 mmoleN m^{-2} , which represents 25% of the surface productivity following this event, 60 mmoleN m^{-2} (days 22 to 32, Fig. 11). In such a case, the actual productivity is thus significantly higher than the productivity estimated from the nutrient depletion budget between the beginning and the end of the experiment. However, such productivity and export events strongly depend on the detail of the forcing variability. The strong wind burst in the high-frequency experiment has a particularly spectacular impact because it happens right after nutrients at the surface have almost entirely been depleted by the biology. A similar wind burst at the beginning of the experiment would have had a much smaller impact.

The decay of the bloom can also be delayed by dynamical inputs of nutrients that occur on smaller space scales, but which still can significantly raise the global productivity budget. On the space and time scales of eddies, it has been shown that mesoscale instabilities have a fertilizing effect, most remarkable during the decay of the bloom, when nutrients become significantly depleted from the surface and vertical nutrient gradients are large. In the case of the *warming* experiment, mesoscale transport sustains up to 40% of productivity, and delays the decay of the bloom by about one week. Other case studies have also emphasized this fertilizing action of eddies, either in oligotrophic conditions (Dadou *et al.*, 1996 ; Flierl and

Davis, 1993 ; McGillicuddy and Robinson, 1997 ; Smith *et al.*, 1996 ; Spall, 1998) or in more eutrophic systems (McGillicuddy *et al.*, 1995 ; Moisan *et al.*, 1996). On the front space scale and wind burst time scale, the Ekman transport induced by the wind can result in a lateral input of nutrients at the surface, and therefore in an increase of productivity. For instance, productivity allowed by the first wind burst in the *high-frequency* experiment is approximately 20 mmoleN m⁻² (days 17 to 20, Fig. 11). Such an enhancement of productivity by Ekman transport of nutrients has also been emphasized by Francks and Walstad (1997).

Primary production and export fluxes must be correctly understood and evaluated, because they control total inorganic carbon content of the mixed layer, which is directly in contact with the atmosphere, and thus influence the carbon dioxide exchange between the ocean and the atmosphere (Longhurst and Harrison, 1989). One of the most remarkable manifestations of the seasonal variability in the world's oceans is the spring phytoplankton bloom in the North Atlantic (Esaias *et al.*, 1986). The greatest oceanic uptake of carbon dioxide happens during this bloom period (Takahashi, 1993), and observations show that it is subject to strong mesoscale and high-frequency variabilities (Watson *et al.*, 1991 ; Yoder *et al.*, 1993 ; Marra, 1995 ; Williams, 1988) . The results of this study emphasize the importance of small scale processes on the productivity and export budget during the bloom in the MEDOC area, and their complex interactions. They can reasonably be extrapolated to the North Atlantic, where winter mixing is also deep. The modelling study of Oschlies and Garçon (1998) supports this extrapolation ; they estimate mesoscale processes to account for 30% of productivity in the North Atlantic. Our results, together with an increasing number of other studies, therefore question the use of coarse resolution, climatological, biogeochemical models of the North Atlantic (Drange, 1994 ; Fasham *et al.*, 1993 ; Sarmiento *et al.*, 1993). We believe that it is necessary to continue in the direction of this work in order to understand, estimate and parameterize the effect, on the large scale, of small scale processes on primary production and export.

Acknowledgments- We thank Anne-Marie Tréguier for valuable discussions. We are grateful to C. Lévy and M. Imbard for their help in computing. We greatly appreciated the help of M. Hood on working on the clarity of the text. Funding for this study was provided by the DRET (Direction des Recherches Etudes et Techniques), CNRS (Centre National de la Recherche Scientifique), MATER (MAST program of EEC) and France-JGOFS (Joint Global Ocean Flux Studies). The computer time was provided by the IDRIS center (Institut du Développement et des Ressources en Informatique Scientifique).

BIBLIOGRAPHY

- Andersen, V. and L. Prieur (1998) High-frequency time series observations in the open northwestern Mediterranean Sea and effects of wind events (DYNAPROC study, May 1995). *Deep-Sea Research*, submitted.
- André, J.-M. (1990) Télédétection spatiale de la couleur de la mer : algorithme d'inversion des mesures du Coastal Zone Color Scanner. Applications à l'étude de la Méditerranée occidentale. PhD, University Paris 6, France.
- André, J.-M. and A. Morel (1991) Atmospheric corrections and interpretation of marine radiances in CZCS imagery, revisited. *Oceanologica Acta*, **14**, 3-22.
- Bisset, W. P., M. B. Meyers, J. J. Walsh and F. E. Müller-Karler (1994) The effects of temporal variability of mixed layer depth on primary productivity around Bermuda. *Journal of Geophysical Research*, **99**, 7539-7553.
- Blanke, B. and P. Delecluse (1993) Variability of the tropical Atlantic Ocean simulated by a general circulation model with two different mixed-layer physics. *Journal of Physical Oceanography*, **23**, 1363-1388.
- Coste, B., J. Gostan and H. J. Minas (1972) Influence des conditions hivernales sur les productions phyto et zooplanctoniques en Méditerranée Nord-Occidentale. I : Structures hydrologiques et distribution de sels nutritifs. *Marine Biology*, **18**, 320-348.
- Dadou, I., V. Garçon, V. Andersen, G. Flierl and C. Davis (1996) Impact of the North Equatorial Current meandering on a pelagic ecosystem : a modeling approach. *Journal of Marine Research*, **54**, 311-342.
- Delecluse, P., G. Madec, M. Imbard and C. Levy (1993) OPA version 7 Ocean general circulation model. internal report LODYC, France.
- Drange, H. (1994) An isopycnic coordinate carbon cycle model for the North Atlantic; and the possibility of disposing of fossil fuel CO₂ in the ocean. PhD, University of Bergen, Norway.

- Eppley, R. W. and E. H. Renger (1988) Nanomolar increase in surface layer nitrate concentration following a small wind event. *Deep-Sea Research*, **35**, 1119-1125.
- Esaias, W. E., G. C. Feldman, C. R. McClain and J. A. Elrod (1986) Monthly satellite-derived phytoplankton pigment distribution for the North Atlantic Ocean basin. *EOS*, **835-837**,
- Fasham, M. J. R., J. L. Sarmiento, R. D. Slater, H. W. Ducklow and R. Williams (1993) Ecosystem behavior at Bermuda station "S" and ocean weather station "India" : a general circulation model and observational analysis. *Global Biogeochemical Cycles*, **7**, 379-415.
- Flierl, G. and C. S. Davis (1993) Biological effects of Gulf Stream meandering. *Journal of Marine Research*, **51**, 529-560.
- Francks, P. J. S. and L. J. Walstad (1997) Phytoplankton patches at fronts : a model of formation and response to wind events. *Journal of Marine Research*, **55**, 1-29.
- Gaillard, F., Y. Desaubies, U. Send and F. Schott (1997) A four-dimensional analysis of the thermal structure in the Gulf of Lion. *Journal of Physical Oceanography*, **102**, 12515-12537.
- Garside, C. and J. C. Garside (1993) The "f-ratio" on 20°W during the North Atlantic Bloom Experiment. *Deep-Sea Research*, **40**, 75-90.
- Gascard, J. C. (1978) Mediterranean deep water formation, baroclinic instability and oceanic eddies. *Oceanologica Acta*, **1**, 315-330.
- Gran, H. H. and T. Braarud (1935) A quantitative study of phytoplankton in the Bay of Fundy and Gulf of Maine. *Journal of Biological Board of Canada*, **I (5)**, 279-467.
- Hitchcock, G. L., C. Langdon and T. J. Smayda (1987) Short term changes in the biology of a Gulf Stream warm-core ring : phytoplankton biomass and productivity. *Limnology and Oceanography*, **32**, 919-928.
- Jacques, G., H. J. Minas, M. Minas and P. Nival (1973) Influence des conditions hivernales sur les productions phyto et zooplanctoniques en Méditerranée Nord-Occidentale. II : Biomasse et production phytoplanctonique. *Marine Biology*, **23**, 251-265.
- Jacques, G., M. Minas, J. Neveux, P. Nival and G. Slawyk (1976) Conditions estivales dans la divergence de Méditerranée Nord-Occidentale. III. Phytoplankton. *Annales de l'Institut Océanographique*, **52**, 141-152.
- Jones, H. and J. Marshall (1997) Restratification after deep convection. *Journal of Physical Oceanography*, **27**, 2276-2287.
- Karrasch, B., H. G. Hoppe, S. Ullrich and S. Podewski (1996) The role of mesoscale hydrography on microbial dynamics in the northeast Atlantic: Results of a spring bloom experiment. *Journal of Marine Research*, **54**, 99-122.
- Klein, P. and B. Coste (1984) Effects of wind-stress variability on nutrient transport into the mixed layer. *Deep-Sea Research*, **31**, 21-37.

- Leaman, K. D. and F. A. Schott (1987) Hydrographic structure of the convection regime in the gulf of Lions : winter 1987. *Journal of Physical Oceanography*, 575-598.
- Lévy, M., L. Mémerly and G. Madec (1998a) The onset of a bloom in the MEDOC area : mesoscale spatial variability. *Deep-Sea Research*, in press.
- Lévy, M., L. Mémerly and G. Madec (1998b) The onset of a bloom after deep winter convection in the North Western Mediterranean sea : mesoscale process study with a primitive equation model. *Journal of Marine Systems*, 16, 7-21. .
- Lévy, M., L. Mémerly and J.-M. André (1998c) New, total and exported productions in the NW Mediterranean Sea : a modelling approach. *Journal of Marine Research*, 56, 197-238.
- Longhurst, A. R. and W. G. Harrison (1989) The biological pump : profiles of plankton production and consumption in the upper ocean. *Progress in Oceanography*, 22, 47-123.
- Madec, G., M. Chartier, P. Delecluse and M. Crepon (1991a) A three-dimentional numerical study of deep water formation in the northwestern mediterranean sea. *Journal of Physical Oceanography*, 21, 1349-1371.
- Madec, G., M. Chartier and M. Crepon (1991b) The effect of thermohaline forcing variability on deep water formation in the Northwestern Mediterranean Sea : a hight-resolution three-dimentional numerical study. *Dynamics of Atmospheres and Oceans*, 15, 301-332.
- Marra, J. (1995) Bioluminescence and optical variability in the ocean: an overview of the Marine Light Mixed Layers program. *Journal of Geophysical Research*, 100, 6521-6525.
- Marra, J., R. R. Bidigare and T. D. Dickey (1990) Nutrients and mixing, chlorophyll and phytoplankton growth. *Deep-Sea Research*, 37, 127-143.
- Marty, J.-C. (1993) Opération DYFAMED, rapport d'activité pour 1993 et programme pour 1994. programme France/JGOFS.
- McGillicuddy, D. J. and A. R. Robinson (1997) Eddy induced nutrient supply and new production in the Sargasso Sea. *Deep-Sea Research*, 44, 1427-1449.
- McGillicuddy, D. J., A. R. Robinson and J. J. McCarty (1995) Coupled physical and biological modelling of the spring bloom in the North Atlantic (II) : three dimentional bloom and post-bloom processes. *Deep-Sea Research*, 42, 1359-1398.
- Medoc group (1970) Observation of formation of deep water in the Mediterranean sea, 1969. *Nature*, 227, 1037-1040.
- Moisan, J. R., E. E. Hofman and D. B. Haidvogel (1996) Modeling nutrient and phytoplankton processes in the California coastal transition zone. 2. A three-dimentional physical-bio-optical model. *Journal of Geophysical Research*, 101, 22677-22691.

- Nival, P., G. Malara, R. Charra and D. Boucher (1972) La matière organique particulaire en Méditerranée occidentale en mars 1970 (chlorophylle, protéines, glucides). Mission "Médiprod II" du Jean-Charcot. *Annales de l'Institut Océanographique*, **48**, 141-156.
- Nival, P., S. Nival and A. Thiriot (1975) Influence des conditions hivernales sur les productions phyto- et zooplanctoniques en Méditerranée nord-occidentale. V : Biomasse et production zooplanctonique - relations phyto-zooplancton. *Marine Biology*, **31**, 249-270.
- Oschlies, A. and V. Garçon (1998) Eddy-induced enhancement of primary production in a model of the North Atlantic Ocean. *Nature*, in press.
- Pedlosky, J. (1987) *Geophysical Fluid Dynamics*, 2nd edition. 710 pp, Springer-Verlag, New-York.
- Robinson, A. R., D. J. McGillicuddy, J. Calman, H. W. Ducklow, M. J. R. Fasham, F. E. Hoge, W. G. Leslie, J. J. McCarthy, S. Podewski, D. L. Porter, G. Saure and J. A. Yoder (1993) Mesoscale and upper ocean variabilities during the 1989 JGOFS bloom study. *Deep-Sea Research*, **40**, 9-35.
- Sarmiento, J. L., R. D. Slater, M. J. R. Fasham, J. R. Ducklow, J. R. Toggweiler and G. T. Evans (1993) A seasonal three-dimensional ecosystem model of nitrogen cycling in the north Atlantic euphotic zone. *Global Biogeochemical Cycles*, **7**, 417-450.
- Smith, C. L., K. J. Richards and M. J. R. Fasham (1996) The impact of mesoscale eddies on plankton dynamics in the upper ocean. *Deep-Sea Research*, **43**, 1807-1832.
- Smolarkiewicz, K. P. and T. L. Clark (1986) The multidimensional positive definite advection transport algorithm : further development and applications. *Journal of Computational Physics*, **67**, 396-438.
- Spall, S. A. (1998) The impact of mesoscale jet activity on plankton heterogeneity and primary production; a numerical modelling study. PhD, University of Southampton.
- Strass, V. H., H. Leach and J. D. Woods (1992) On the seasonal development of mesoscale variability : the influence of the seasonal pycnocline formation. *Deep-Sea Research*, **39**, 1627-1639.
- Sverdrup, H. U. (1953) On Conditions for the Vernal Blooming of Phytoplankton. *J. Cons. Int. Expor. Mer.*, **18**, 287-295.
- Takahashi, T. (1993) Seasonal variations of CO₂ and nutrients in the high-latitude surface oceans: a comparative study. *Global Biogeochemical Cycles*, **7**, 843-878.
- Townsend, D. W., L. M. Cammen, P. M. Holligan, D. E. Campbell and N. R. Pettigrew (1994) Causes and consequences of variability in the timing of spring phytoplankton blooms. *Deep-Sea Research*, **41**, 747-765.

- Townsend, D. W., M. D. Keller, M. E. Sieracki and S. G. Ackleson (1992) Spring phytoplankton blooms in the absence of vertical water column stratification. *Nature*, **360**, 59-62.
- Watson, A. J., C. Robinson, J. E. Robinson, P. J. I. B. Williams and M. J. R. Fasham (1991) Spatial variability in the sink for atmospheric carbon dioxide in the North Atlantic. *Nature*, **350**, 50-53.
- Williams, R. (1988) Spatial heterogeneity and niche differentiation in oceanic zooplankton. *hydrobiologia*, **167-168**, 151-159.
- Williams, R. G. and M. J. Follows (1998) The Ekman transfer of nutrients and maintenance of new production over the North Atlantic. *Deep-Sea Research*, **45**, 461-489.
- Webb, W. L., M. Newton and D. Starr (1974) Carbon dioxide exchange of *Alnus Rubra* : a mathematical model. *Ecologia*, **17**, 281-291.
- Yoder, J. A., J. Aiken, R. N. Swift, F. E. Hoge and P. M. Stegmann (1993) Spatial variability in near-surface chlorophyll a fluorescence measured by the Airbone Oceanographic Lidar (AOL). *Deep-Sea Research*, **40**, 33-53.

Table 1.

Atmospheric forcings used for the no flux, the warming, the wind and the high-frequency experiments : penetrative solar radiation, non-solar heat budget and wind stress. See text for more details.

	Solar heat flux	Non-solar heat flux	Wind stress
no flux	150 W m^{-2}	-150 W m^{-2}	0
warming	$150 \text{ W m}^{-2} + 2 \text{ W m}^{-2}\text{d}^{-1}$	-150 W m^{-2}	0
wind	150 W m^{-2}	-150 W m^{-2}	0.15 Pa
high frequency	ECMWF 1990 data (Fig. 1)		

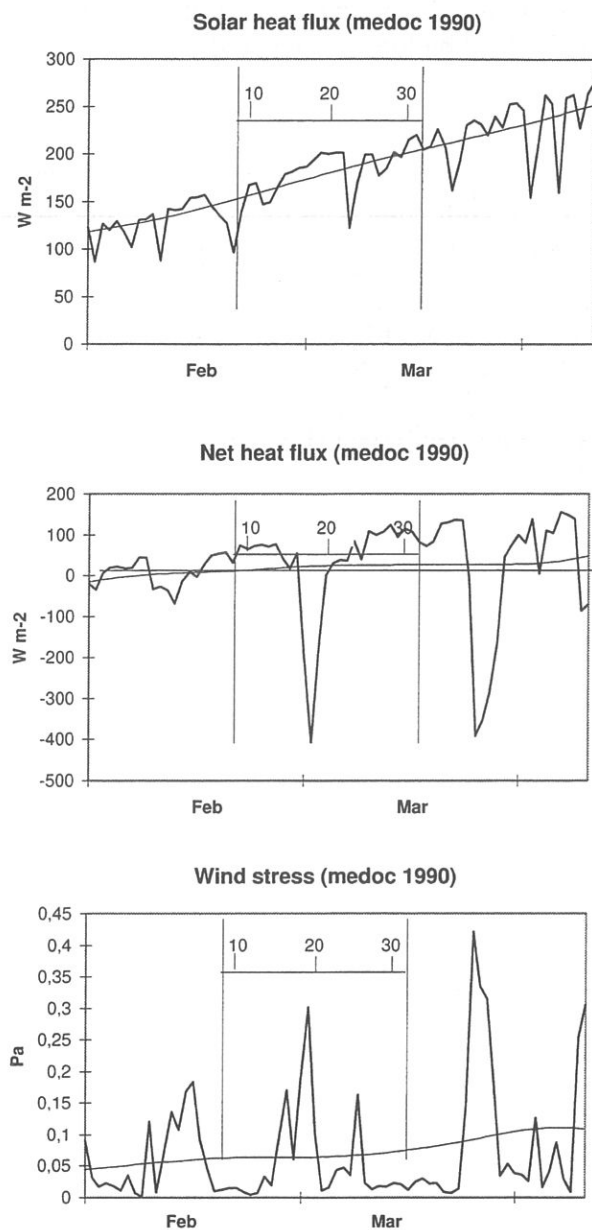


Figure 1.

Daily solar heat flux, net heat flux and wind stress over the MEDOC area predicted by the European Center for Medium Weather Forecast (ECMWF) for February and March 1990 (thick black lines). The solar radiation shows a continuous increase during the period. Two strong wind bursts (end of February and end of March) are associated with strong heat losses. The superimposed thin lines show the monthly smoothing of these data. The two vertical lines delimit the temporal window of the *high-frequency* experiment (Feb., 20 until March, 15, corresponding to days 8 to 33 of the experiment).

Figure 2.
Time series of the surface density field (relatively to $\sigma_\theta=28.0$) for the *no flux*, the *warming* and the *wind* experiments. Contour interval is 0.05 in units of σ_θ . Only a zoom of the domain is represented. The gray scale emphasizes the progressive warming of the surface waters in the *warming* experiment.

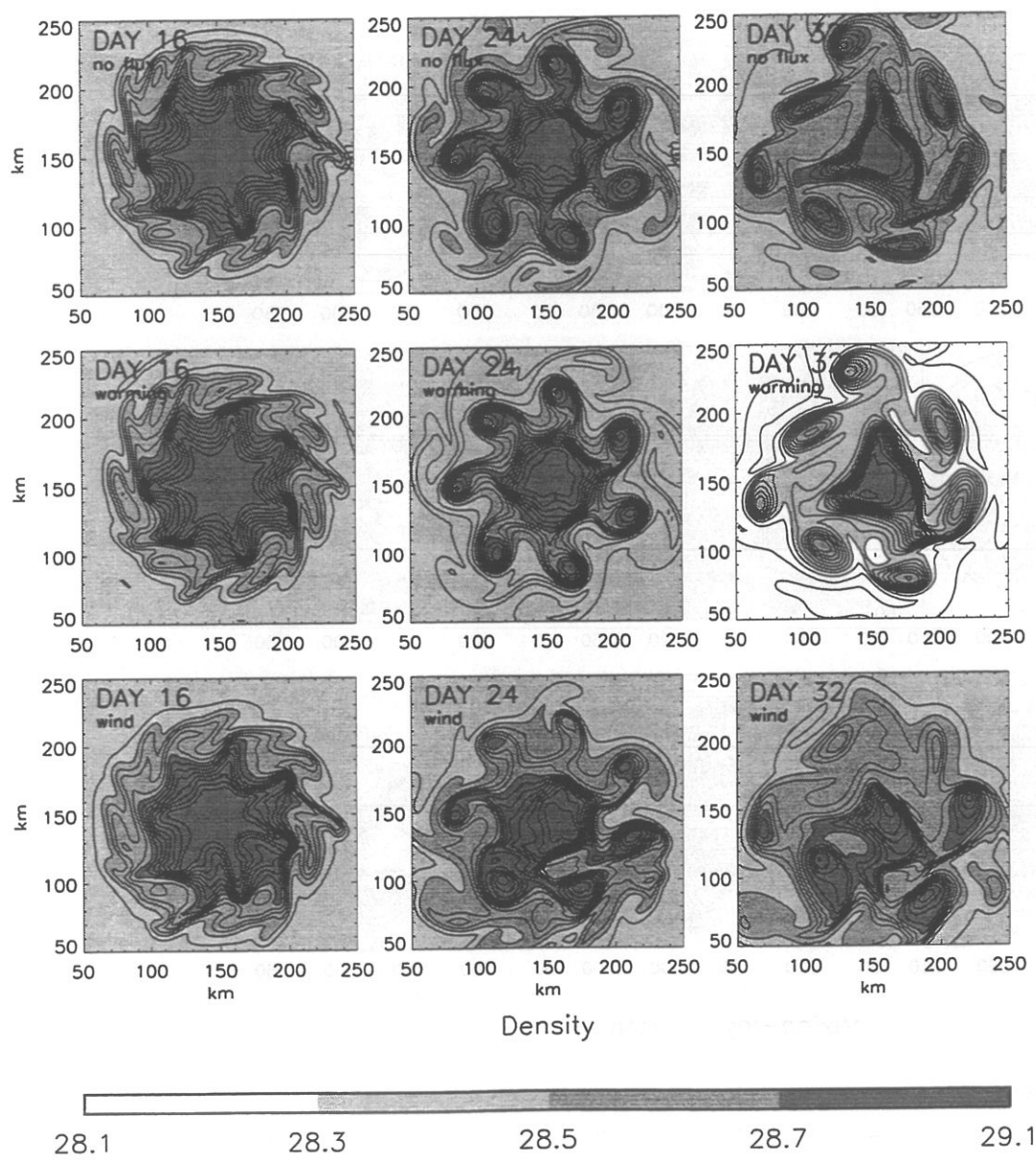


Figure 3.

Mixing-layer depth time series for the *no flux*, the *warming* and the *wind* experiments. The mixing layer is defined as the surface layers where the vertical mixing coefficient is greater than $10^{-4} \text{ m}^2 \text{ s}^{-1}$. As this coefficient exhibits a sharp vertical variation at the bottom of the mixing layer, this definition is quite insensitive to the minimum value chosen, as long as it is reasonable (between $5 \cdot 10^{-4}$ and $5 \cdot 10^{-3} \text{ m}^2 \text{ s}^{-1}$).

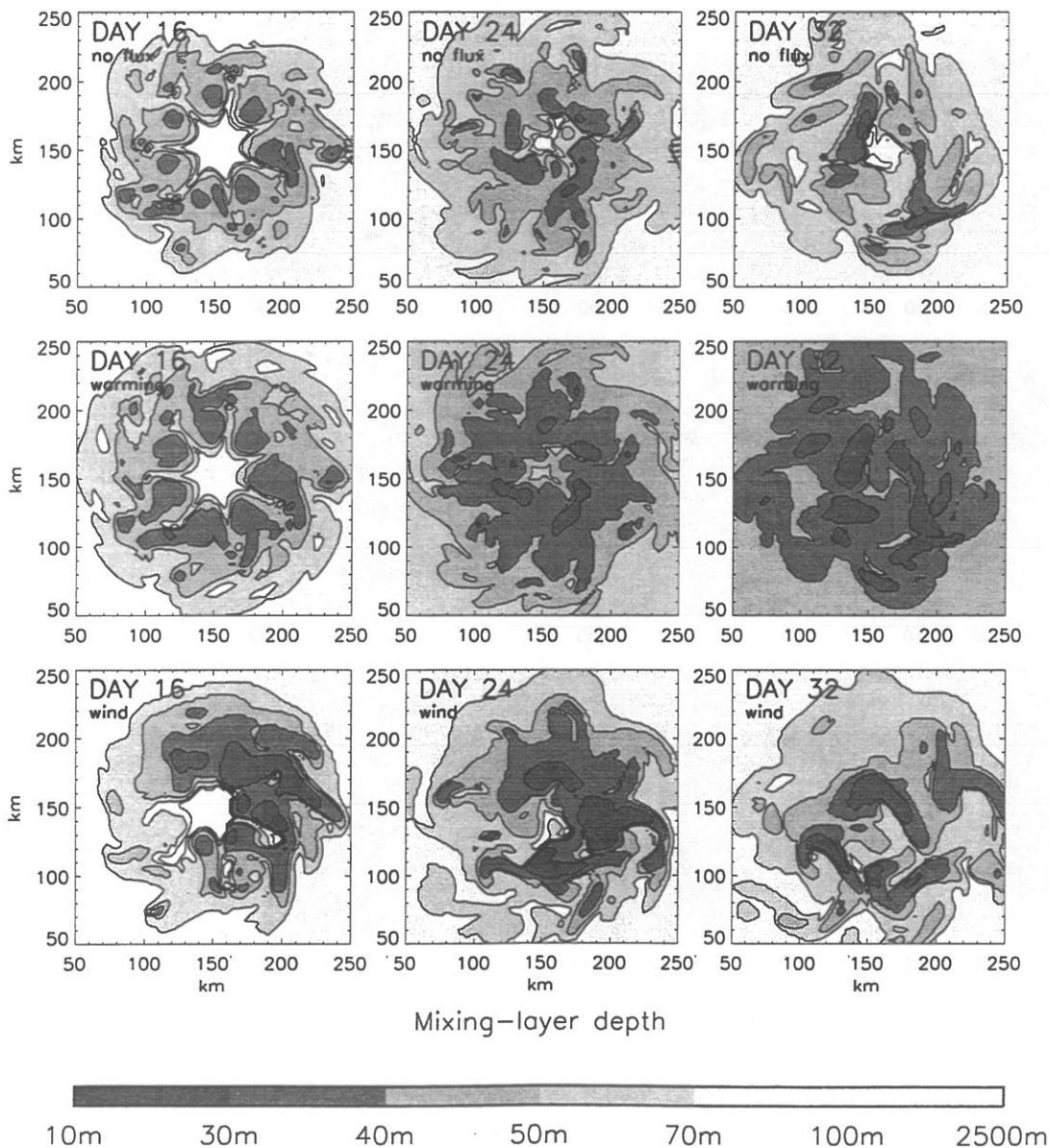
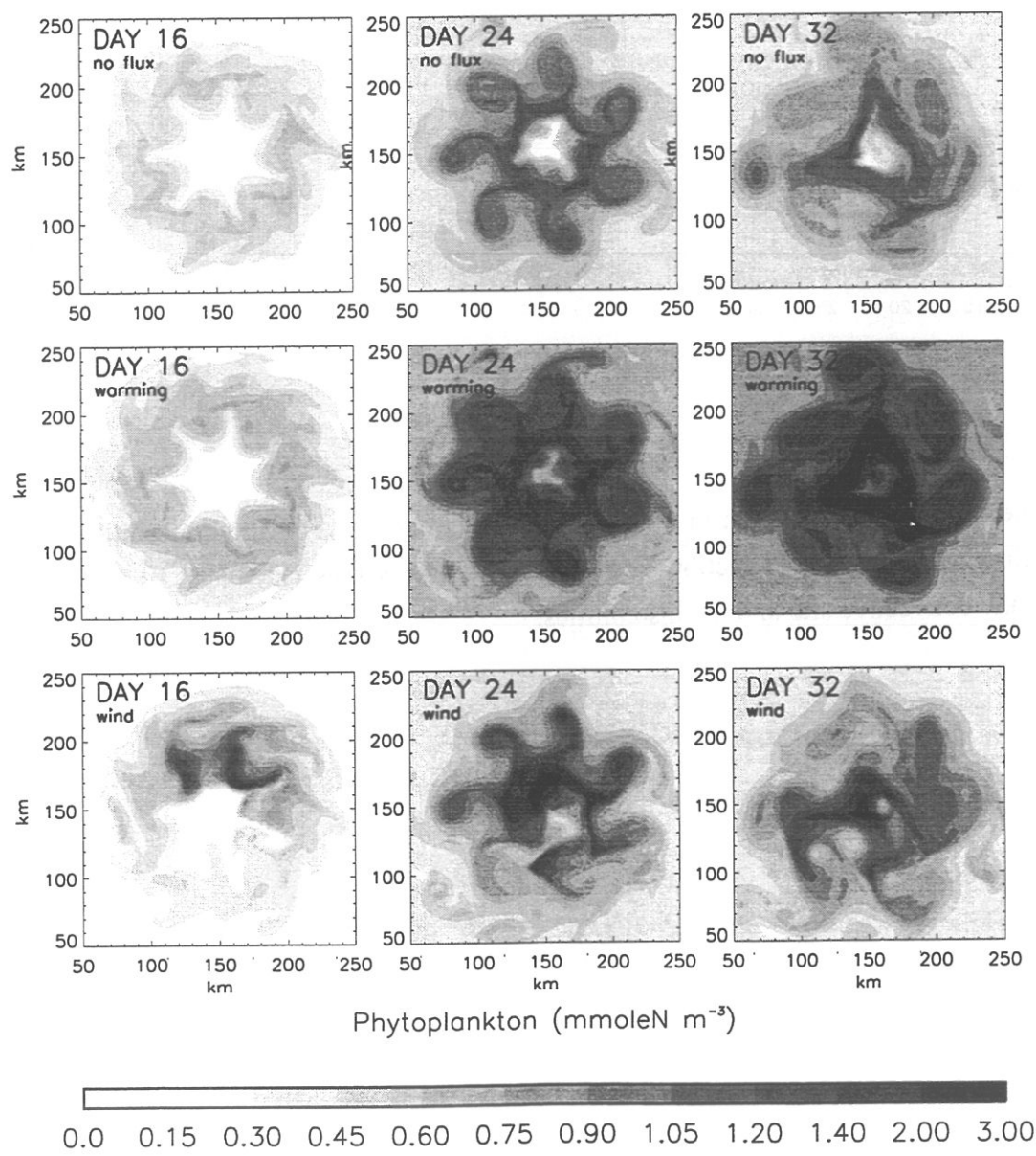


Figure 4.
Surface phytoplankton concentration time series for the *no flux*, the *warming* and the *wind* experiments. Note that the gray scale is not linear.



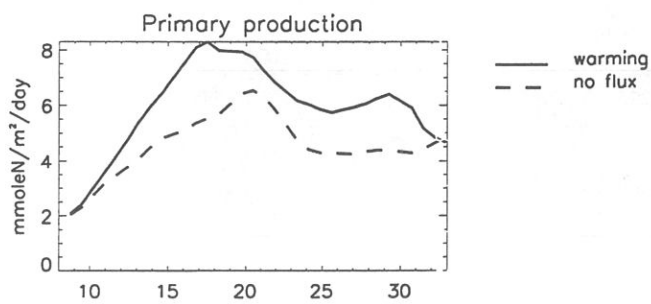
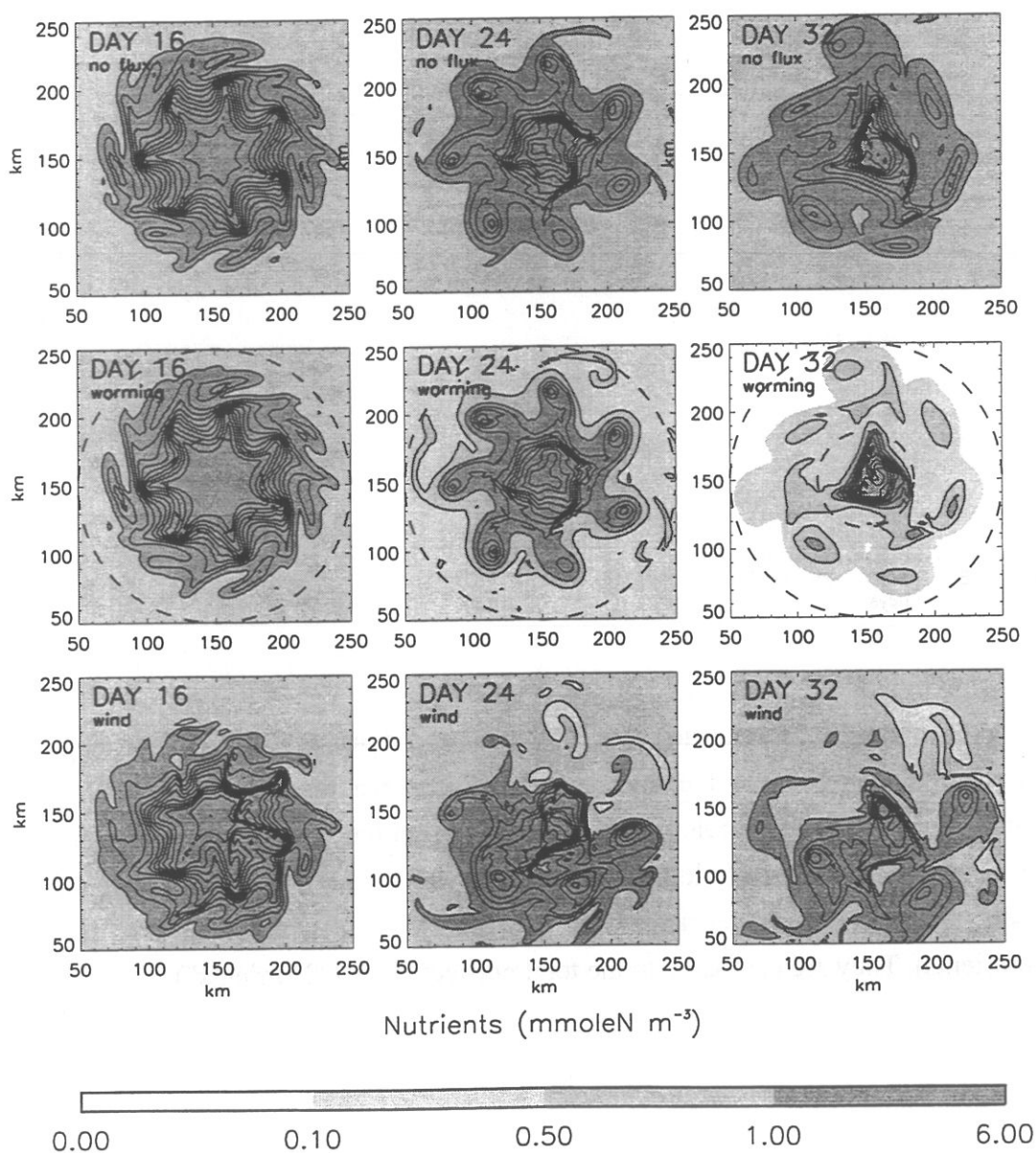


Figure 5.

Average over the circular area centered in the center of the domain and of 100 km radius of the 0-100 m cumulated primary production. The spatial average is thus calculated over the area that covers the convective site and the instabilities.

Figure 6.

Surface nutrient concentration time series for the *no flux*, the *warming* and the *wind* experiments. The contour interval is $0.5 \text{ mmoleN m}^{-3}$. The dotted circles delimit the instability area, over which diagnostics pictured in Figure 7 are averaged.



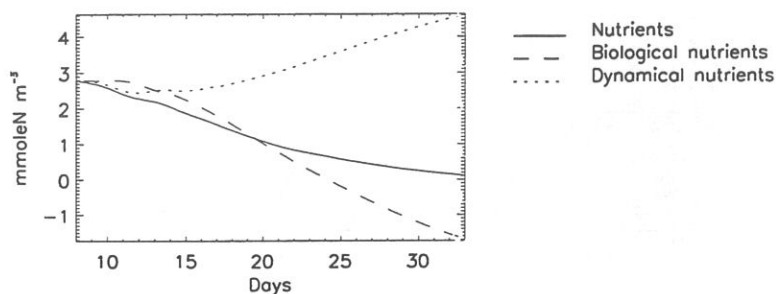


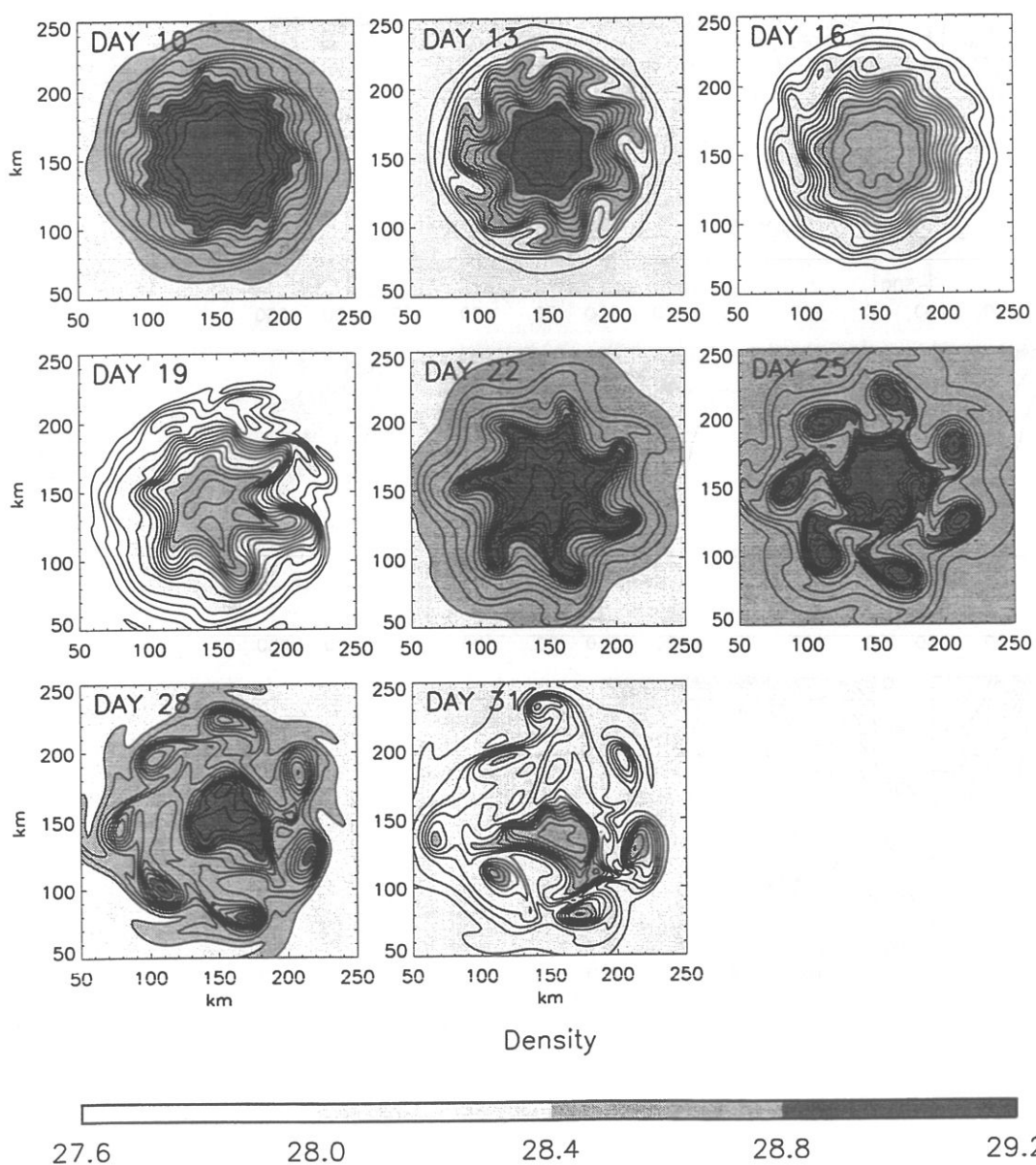
Figure 7.

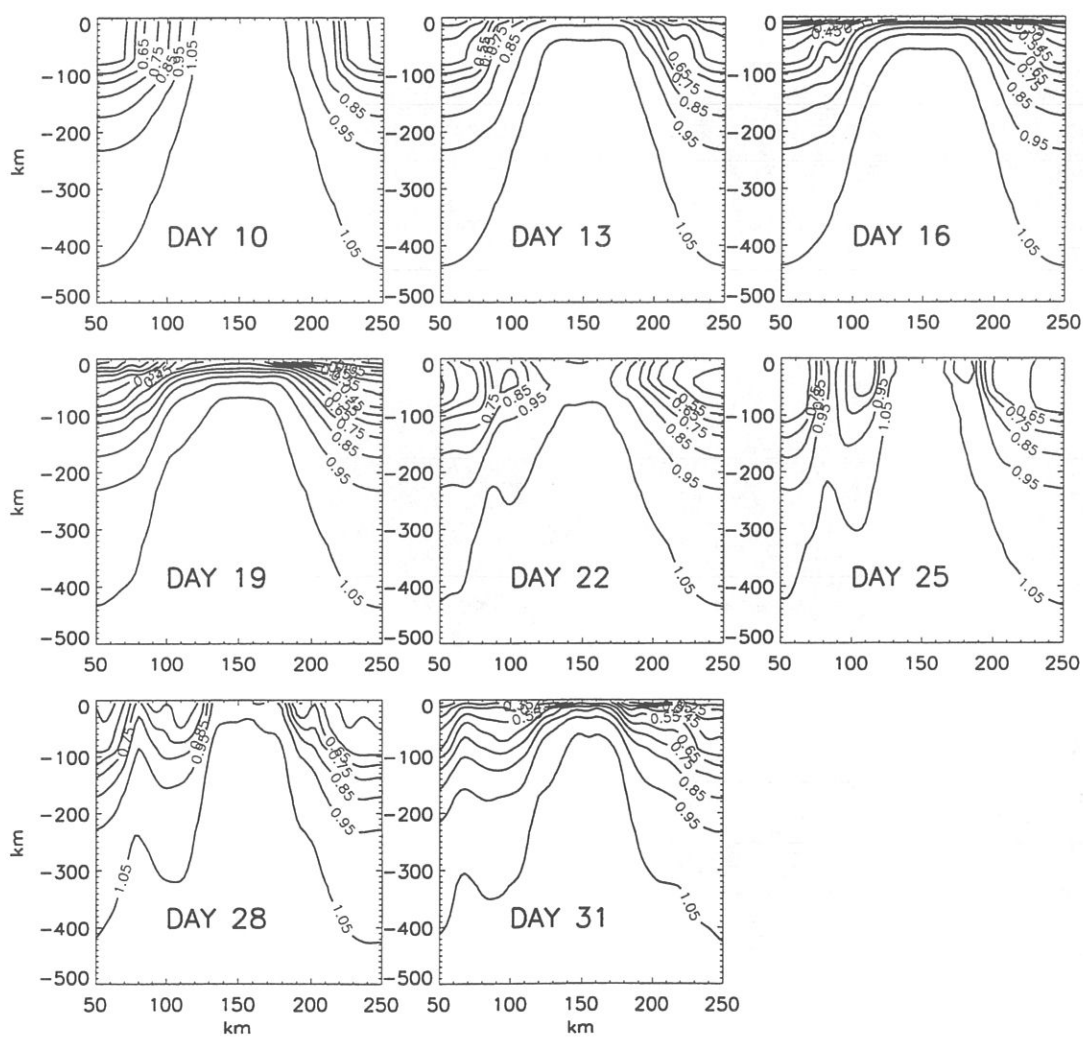
For the surface layer, nutrient concentration and biological and dynamical nutrient forcings integrated with time, integrated over the area comprised between the two dotted circles pictured in Figure 6. Time integrated biological forcings represent the amount of nutrient that is locally taken up by the biology ("Biological" nutrients), while time integrated dynamical forcings represent the amount of nutrients that is imported by dynamical processes ("Dynamical" nutrients). They are compared to the total nutrient stock ("Nutrients").

Figure 8.

a- Surface density time series (relatively to $\sigma_\theta=28.0$) for the *high-frequency* experiment. Contour interval is 0.05 in units of σ_θ .

b- Density section (across $y=150$ km) time series for the *high-frequency* experiment. Contour interval is 0.1 in units of σ_θ .





b)

Figure 9.

Mixing-layer depth time series for the *high-frequency* experiment. Contour intervals superimposed on the gray scale are 10, 20, 40, 60 and 80 m.

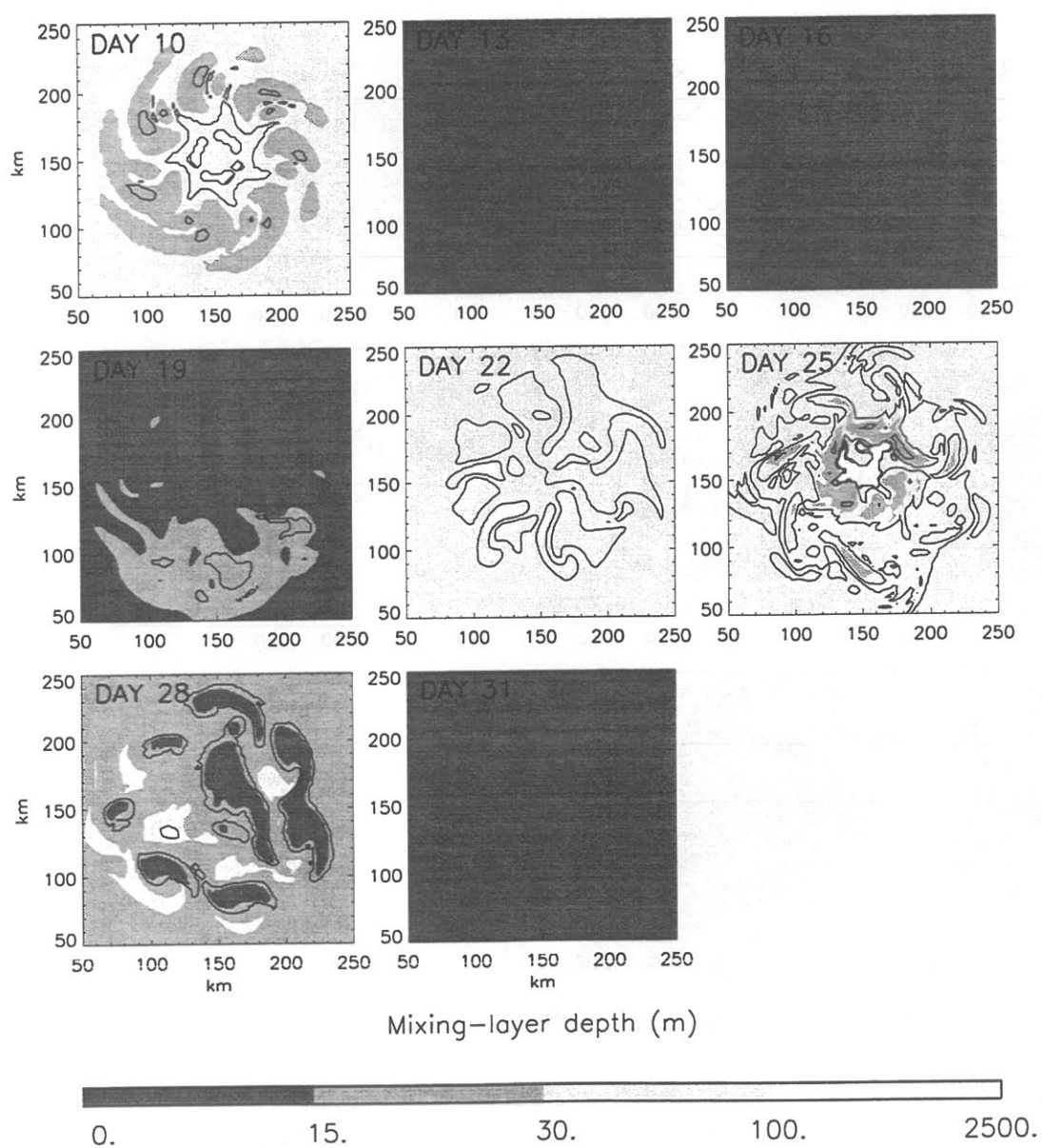
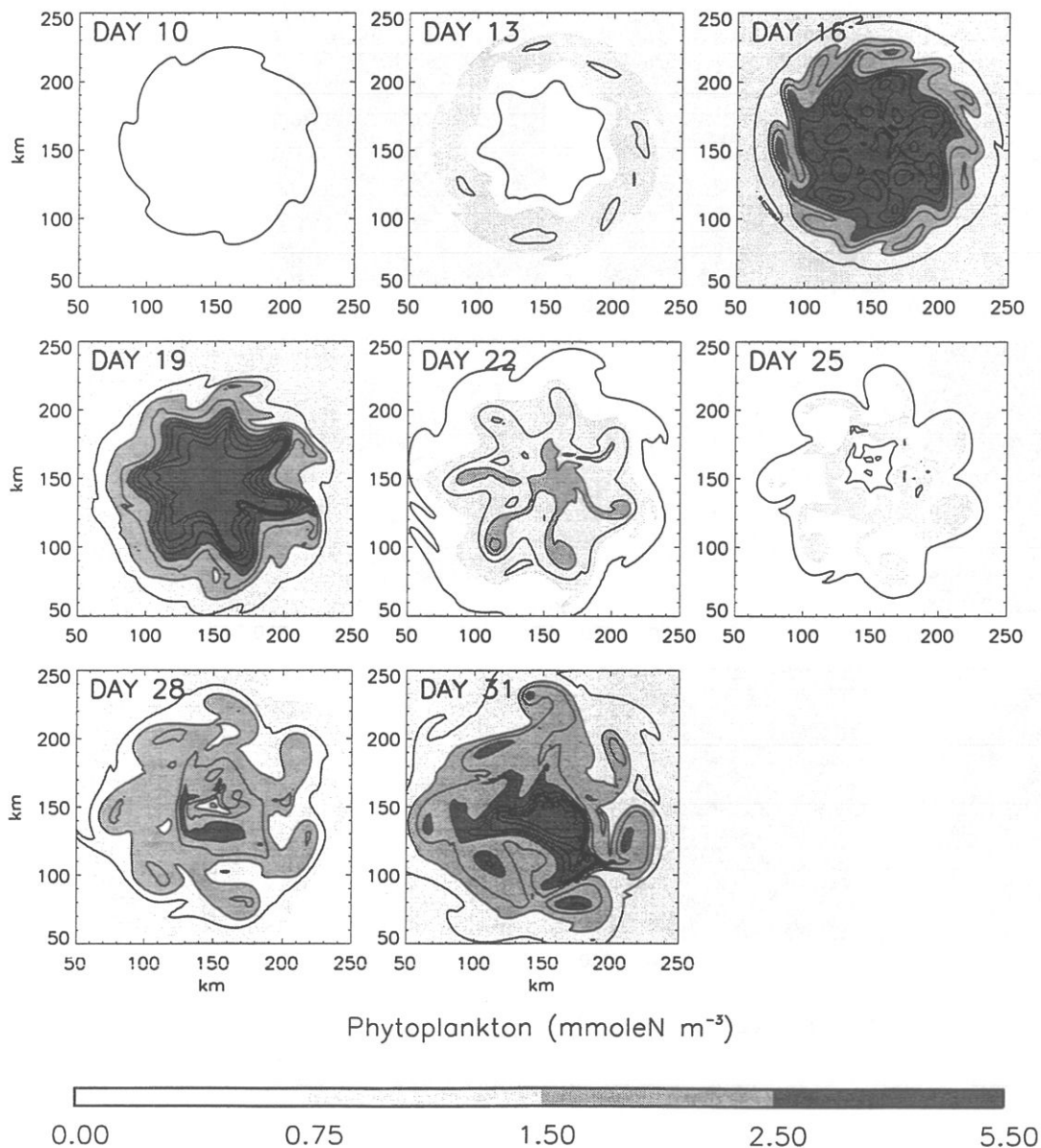
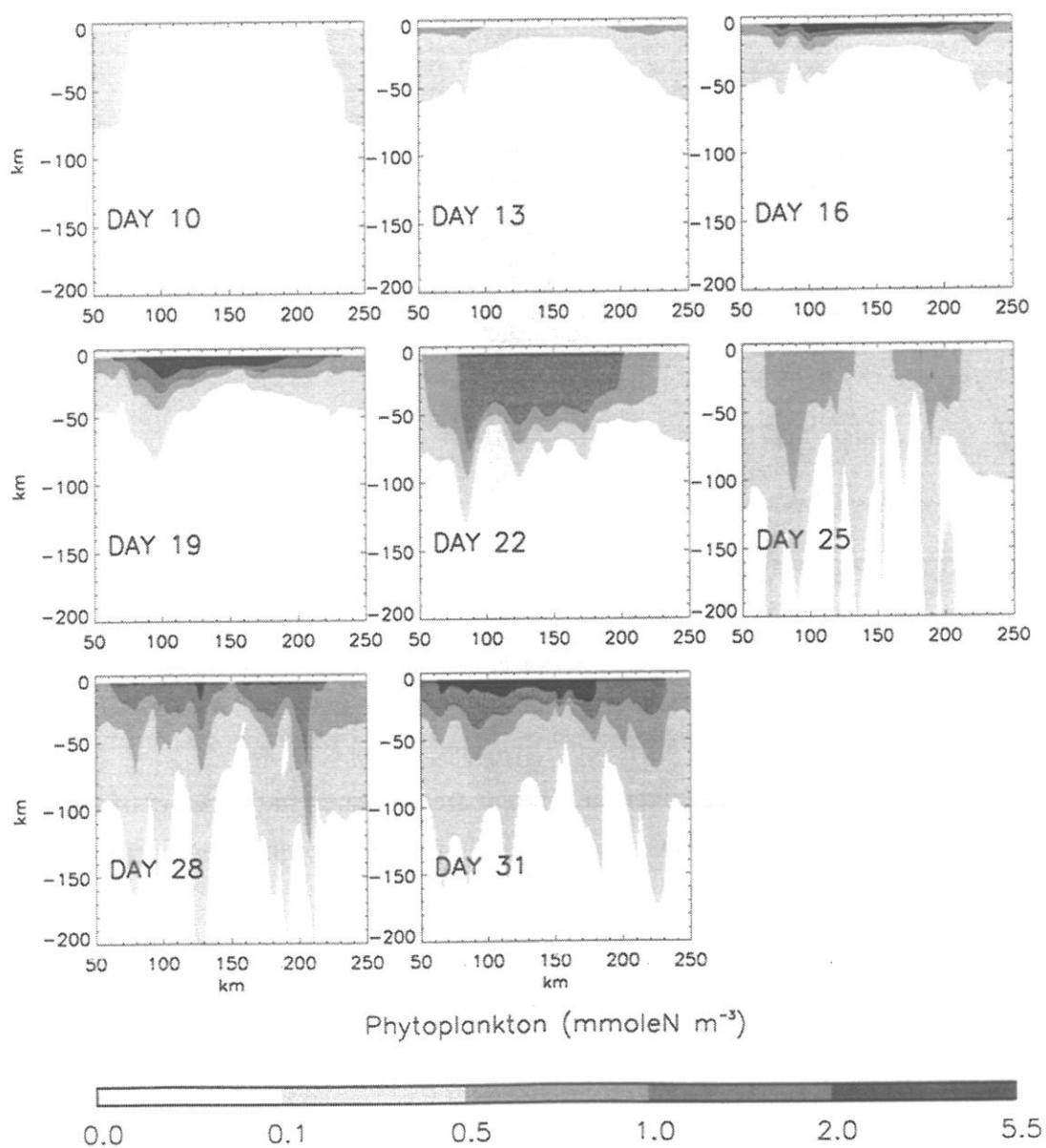


Figure 10.

- a- Surface phytoplankton concentration time series for the *high-frequency* experiment. Contour intervals superimposed on the gray scale are 0.5 mmoleN m⁻³.
- b- Phytoplankton section (across y=150 km) time series for the *high-frequency* experiment. Note that the gray scales are different on Figures 10a and 10b.





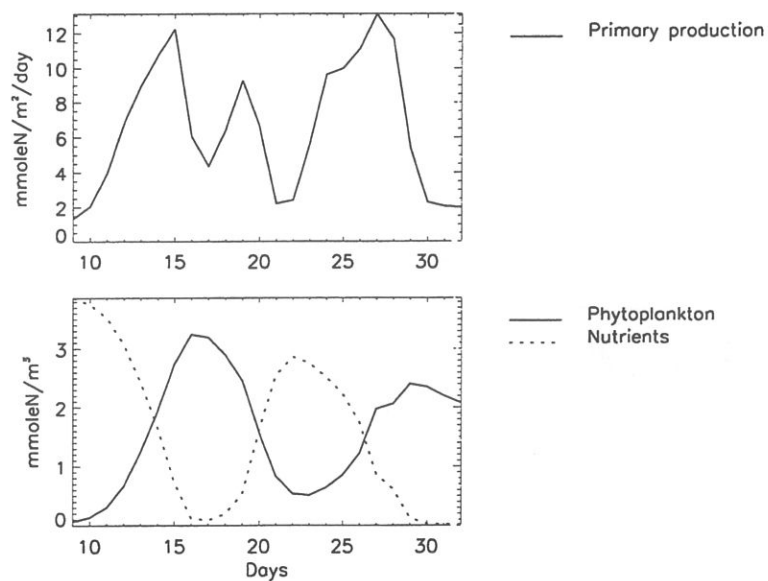


Figure 11.

For the *high-frequency* experiment, average over the circular area centered in the center of the domain and of 100 km radius of 0-100 m cumulated primary production, surface phytoplankton and surface nutrients.

APPENDIX : THE NPZD BIOGEOCHEMICAL MODEL

The NPZD primary production model used in this study is a simplified version of the BIOMELL biogeochemical model developed in a one-dimensional vertical framework by Lévy *et al.* (1998c) for the northwestern Mediterranean seasonal cycle of primary production and export fluxes. The simplification mostly concerns the regeneration and the export pathways. It was made possible by the fact that the simplified model was designed to study the winter and spring periods, when regeneration and exports are weak.

The resulting NPZD model consists of four prognostic variables (instead of ten) expressed in terms of their nitrogen content : nutrients (N), phytoplankton (P), zooplankton (Z) and detritus (D). The biogeochemical source/sink budgets for each of the variables are (with model parameters in Table 1) :

$$S(N) = -\mu_p L_I L_N P + \mu_z Z + \mu_d D \quad (1)$$

$$S(P) = \mu_p L_I L_N P - G_p - m_p P \quad (2)$$

$$S(Z) = a_p G_p + a_d G_d - \mu_z Z - m_z Z \quad (3)$$

$$S(D) = (1 - a_p) G_p + (1 - a_d) G_d + m_p P + m_z Z - \mu_d D - G_z^d - V_d \partial_z D \quad (4)$$

The formulation for phytoplankton growth (i.e. primary production, $\mu_p L_I L_N P$) takes into account nutrient and light limitations. Nutrient limitation has the Michaelis-Menten kinetics ($L_N = N/(N + K_N)$). Light limitation has the Webb *et al.* (1974) type ($L_I = \gamma_m (1 - e^{-\overline{\text{PAR}}/K_{\text{PAR}}})$), modulated by a parameterization of lagrangian production inhibition in situations of deep mixing through a specific coefficient γ_m . γ_m is set to 1 (no limitation) when the mixing layer is shallower than the euphotic layer. In such a case, cells within the mixing layer are assumed to experience a mean photosynthetic available radiation $\overline{\text{PAR}}$ over the mixing layer. When the mixing layer becomes deeper than the euphotic layer, γ_m decreases accordingly down to a threshold value of 0.1, and $\overline{\text{PAR}}$ is taken as the averaged photosynthetic available radiation over the euphotic layer (computed as the 1% incident light depth). This parameterization has been proposed by André (1990) and yielded encouraging results in the one-dimensional study of Lévy *et*

al. (1998c) in the northwestern Mediterranean Sea. It is based on considerations on the light experienced by the phytoplankton cells during their doubling time, which is a purely lagrangian aspect.

Grazing of phytoplankton and detritus is formulated following Fasham *et al.* (1990) :

$$G_p = g_z Z \frac{P^2}{(P + D)K_z + P^2 + D^2} \quad (5)$$

$$G_d = g_z Z \frac{D^2}{(P + D)K_z + P^2 + D^2} \quad (6)$$

The other biogeochemical interactions taken into account are phytoplankton mortality, zooplankton mortality and zooplankton excretion (these last two processes are inhibited when zooplankton concentration is below a given threshold), fecal pellet production, detritus sedimentation and detritus remineralisation.

The photosynthetic available radiation (*PAR*) is derived from a light absorption model. Only a fraction of the light field (43%) can be used for photosynthesis. Two different light wavelength are considered. The absorption coefficients depend on the local phytoplankton concentrations :

$$\lambda_r = \lambda_{r0} + \lambda_{rp} Chl^{l_r} \quad (7)$$

$$\lambda_g = \lambda_{g0} + \lambda_{gp} Chl^{l_g} \quad (8)$$

$$Chl = 12 P R_{c:n} / R_{pig} R_{c:chl} \quad (9)$$

$$PAR_r(z=0) = PAR_g(z=0) = 0,43 Q_{sol} / 2 \quad (10)$$

$$PAR_r(z) = PAR_r(z - \Delta z) e^{-\lambda_r \Delta z} \quad (11)$$

$$PAR_g(z) = PAR_g(z - \Delta z) e^{-\lambda_g \Delta z} \quad (12)$$

$$PAR(z) = PAR_r(z) + PAR_g(z) \quad (13)$$

The equations for the biogeochemical model are solved for the uppermost twelve model levels (~200 m). Below, the three biogenic compartments decay to nutrients, with a decaying rate varying from one to twenty days.

Table 1 : parameters for the NPZD model

Nutrient half-saturation constant	K_n	0.5	mmole/m ³
Phytoplankton maximal growth rate	μ_p	2	d ⁻¹
Carbon/Chlorophyll ratio	R_{c-chl}	55	gC/gChl
Half-saturation constant for light	K_{PAR}	33.33	W/m ²
Phytoplankton mortality rate	m_p	0.03	d ⁻¹
Zooplankton maximal grazing rate	g_z	0.75	d ⁻¹
Half-saturation constant for grazing	K_z	1	mmole/m ³
Assimilated fraction of phytoplankton	a_p	0.7	
Assimilated fraction of detritus	a_d	0.5	
Excretion rate	μ_z	0.1	d ⁻¹
Mortality rate	m_z	0.03	d ⁻¹
Threshold for zooplankton losses	Z_{min}	0.015	mmole/m ³
Detritus sedimentation speed	V_d	5	m d ⁻¹
Detritus remineralisation rate	μ_d	0.09	d ⁻¹
Water absorption in red	λ_{r0}	0.225	m^{-1}
Water absorption in blue	λ_{g0}	0.0232	m^{-1}
Pigments absorption in red	λ_{rp}	0.037	$m^{-1} (mgChl / m^3)^{-l_r}$
Pigments absorption in blue	λ_{gp}	0.074	$m^{-1} (mgChl / m^3)^{-l_g}$
Power law for absorption in red	l_r	0.629	
Power law for absorption in blue	l_g	0.674	
Contribution of Chlorophyll to absorbing pigments	R_{pig}	0.7	

Déjà paru :

- 1 : **Janvier 1998** Agnès Ducharne, Katia Laval and Jan Polcher,
Sensitivity of the hydrological cycle to the parameterization of soil hydrology in a GCM
- 2 : **Janvier 1998** Marina Lévy, Laurent Mémerly and Jean-Michel André ,
Simulation of primary production and export fluxes in the Northwestern Mediterranean Sea
- 3 : **Février 1998** Valérie Masson, Sylvie Joussaume, Sophie Pinot and Gilles Ramstein, *Impact of parameterizations on simulated winter mid-Holocene and Last Glacial Maximum climatic changes in the Northern Hemisphere*
- 4 : **Mars 1998** Jérôme Vialard et Pascale Delecluse, *An OGCM Study for the TOGA Decade. Part I: Role of Salinity in the Physics of the Western Pacific Fresh Pool, Part II: Barrier layer formation and variability*
- 5 : **Avril 1998** O. Aumont, J. C. Orr, P. Monfray, and G. Madec, *Nutrient trapping in the equatorial Pacific: The ocean circulation solution*
- 6 : **Mai 1998** Emmanuelle Cohen-Solal and Hervé Le Treut, *Long term climate drift of a coupled surface ocean-atmosphere model : role of ocean heat transport and cloud radiative feedbacks*

